npj | breast cancer

Article

Published in partnership with the Breast Cancer Research Foundation

https://doi.org/10.1038/s41523-026-00917-0

The landscape of B and plasma cells in breast cancer: insights from single-cell and spatial transcriptomics

Xing Cai[1,2,3,7], Jinru Yang[4,7], Wenzheng Wang[1,2,7], Xiaolu Zhan[1,2], Xiaohan Chen[1,2], Dongchen Ji[1,2], Kexin Liu[1,2], Xue Li[1,2], Yuxin Zhang[1,2], Cheng Qian[1,2] ✉, Xiaofang Dai[3,5,6] ✉, Guang Yang[1,2] ✉ & Tong Liu[1,2] ✉

Tumor-associated B (TAB) cells and plasma cells are increasingly recognized as key components of the tumor microenvironment; however, their heterogeneity and functional roles in breast cancer remain incompletely understood. Here, by integrating publicly available single-cell RNA (scRNA) sequencing datasets with newly generated scRNA-seq and single-cell BCR sequencing data from 79 samples across 35 patients, we constructed a comprehensive atlas of B and plasma cells in breast cancer. Systematic analyses of transcriptional profiles, clonal expansion, spatial distribution, and cell-cell interactions revealed 21 distinct subsets of TAB cells with substantial functional diversity. Among them, two tumor-enriched populations, $CD200^+$ naïve B cells and $ISG15^+$ atypical memory B cells, exhibited marked clonal expansion and activation signatures. Notably, $CD200^+$ naïve B cells were closely associated with tertiary lymphoid structures, improved clinical outcomes, and enhanced responses to immune checkpoint blockade. Functional validation in multiple murine tumor models demonstrated that $CD200^+$ B cells are essential for optimal anti-tumor immunity and critical for the efficacy of anti-PD-1 therapy. Together, our findings provide a high-resolution landscape of B and plasma cells in breast cancer and highlight $CD200^+$ tumor-associated B cells as promising biomarkers and potential therapeutic targets to improve immunotherapy outcomes.

Cancer immunotherapy's remarkable success has sparked a comprehensive exploration of the tumor ecosystem, with a particular emphasis on immune components within the tumor microenvironment (TME). However, research has predominantly focused on the heterogeneity and functional dynamics of tumor-infiltrating T cells and myeloid cells[1,2]. Other types of cells, especially tumor-associated B cells (TABs)[3] and plasma cells (PC), have largely been overlooked, and their pathogenic role in solid tumors like breast cancer (BRCA) remains poorly understood. TABs can be detected in various types of solid tumors[4]. Recent research, including studies conducted by our group and others, has demonstrated that TABs are crucial in shaping patients' anticancer chemotherapy and immunotherapy responses, also influencing clinical outcomes in melanoma and gastric cancer, etc.[5–7].

To fully unlock human cancer immunosurveillance potential, an extensive understanding of the TME is essential. B cells are a vital part of the adaptive immune system, serving a central role in regulating humoral immunity. In the TME, TABs exhibit a high degree of functional heterogeneity, encompassing different subtypes from naïve B cells (Bn), germinal center (GC) B cells, memory B cells (Bm), to antibody-secreting cells (ASCs), including plasma cells (PCs) and plasmablasts (PBs), which are classified mainly based on their immunophenotypes. Recent studies have also shown that B cells have the potential for next-generation immunotherapies, demonstrating their ability toproduce antibodies targeting tumor-associated antigens (TAA), enhance phagocytosis, and present antigens to $CD8^+$T cells. Studies have demonstrated that in renal carcinoma (RC) and ovarian carcinoma (OV), terminally differentiated B cells (PCs) produce anti-tumor antibodies, aiding in the elimination of cancer cells[7,8]. However, TABs also exhibit tumor-promoting properties, including cytokine release, immune complex formation, and involvement in immune

[1]Department of Oncological Surgery, Harbin Medical University Cancer Hospital, Harbin, PR China. [2]NHC Key Laboratory of Cell Transplantation, The First Affiliated Hospital of Harbin Medical University, Harbin, PR China. [3]Hubei Key Laboratory of Precision Radiation Oncology, Wuhan, PR China. [4]Department of Radiation and Medical Oncology, Zhongnan Hospital of Wuhan University, Wuhan, PR China. [5]Cancer Center, Union Hospital, Tongji Medical College, Huazhong University of Scienceand Technology, Wuhan, PR China. [6]Institute of Radiation Oncology, Union Hospital, Tongji Medical College, Huazhong, University of Science and Technology, Wuhan, PR China. [7]These authors contributed equally: Xing Cai, Jinru Yang, Wenzheng Wang.
✉e-mail: qiancheng@ems.hrbmu.edu.cn; 2003xh1047@hust.edu.cn; guangyang@hrbmu.edu.cn; liutong@hrbmu.edu.cn

checkpoint regulation. Additionally, TABs closely interact with other immune cells in the tumor microenvironment, as evidenced by the co-occurrence of B cell accumulation with the spatial clustering of diverse immune populations and the formation of tertiary lymphoid structures (TLSs)[7,9]. These TLSs serve as hubs for B cell maturation and enhance anti-tumor responses. Additionally, increasing evidence indicates that B cells are increasingly recognized as prognostic markers across multiple cancer types, although their roles vary significantly depending on the cancer type[10–12]. The connection between B cells and immunotherapy responsiveness underscores their clinical significance[13]. Notably, TLSs have emerged as strong predictive biomarkers for the efficacy of cancer immunotherapy[14–16]. While pan-cancer TAB datasets provide a detailed characterization of B cell differentiation across most cancers, the insufficient number of sequenced B cells in each cancer type may hinder the detection of rare subsets. These results highlight the dual functions of B cells in cancer, where they may both promote anti-tumor responses and drive tumor progression. However, the heterogeneity and function of B cells in breast cancer remain unclear.

In this research, we collected publicly available single-cell RNA-sequencing (scRNA-seq) datasets of the TME in BRCA and combined them with our paired scRNA-seq and single-cell BCR sequencing (scBCR-seq) data from 79 samples across 35 patients to construct a comprehensive atlas of breast cancer-associated B cells. We analyzed the function and heterogeneity of these B cells with unprecedented resolution, exploring their transcriptional profiles, differentiation and maturation stages, spatial distribution, clonal characteristics, and their co-localization and cellular interactions patterns with other cell populations within the TME. We also linked $CD200^{+}$TABs features with immunotherapy and clinical prognosis and experimentally evaluated their potential to synergistically enhance immunotherapy outcomes. This research provides detailed insights into the universal properties of B cells in the development of BRCA.

Results

Single-cell analysis reveals the heterogeneity of B cell populations in breast cancer

B cell infiltration exhibits significant transcriptional variation across different human cancer types, and its status in BRCA remains largely unexplored. To investigate the infiltration patterns of B cells in BRCA, we conducted combined scBCR-seq and scRNA-seq on cells acquired from 79 BRCA samples, including matched tumor tissues, ANTs, lymph node metastases (LM), and peripheral blood (Fig. 1A, Supplementary Fig. 1A and Supplementary Table 1). Additionally, we integrated various published datasets containing TABs and ultimately constructed a single-cell transcriptional atlas from 409 samples. A high-resolution single-cell transcriptome map was generated, consisting of 107,921 B cells from 409 samples, primarily derived from tumor tissues, ANTs, LM, and blood. All scRNA-seq datasets were integrated, and batch effects were corrected using fastMNN[17] (Supplementary Fig. 1B). Unsupervised clustering identified five primary clusters corresponding to distinct B cell lineages: Bm cells, Bn cells, B_GC cells, and PCs (Fig.1B). These clusters were characterized by the high expression of canonical markers, including TCL1A/IGHD for Bn cells, TNFRSF13B/CD27 for Bm cells, AICDA/BCL6 for B_GC cells, MZB1 and MKI67 for PCs (Supplementary Fig. 1C).

We then performed further clustering on the four major clusters mentioned above and identified 21 distinct B cell subtypes, each characterized by specific marker genes (Supplementary Fig. 2A–F). To further elucidate the molecular phenotypes of these B cell subsets, we employed gene set-based analyses (Fig. 1C). For Bm cells, four subtypes were identified, including C4_Bm_FGR and C5_Bm_ISG15, both of which exhibited transcriptional phenotypes consistent with atypical B cells (ABCs). C4_Bm showed high expression of FGR, while C5_Bm was characterized by elevated expression of interferon (IFN) -stimulated genes (Supplementary Fig. 2B, E). ABCs have been described in a prior study on infections, autoimmune diseases, and vaccination[18–20]. Both C4 and C5 Bm subtypes demonstrated ABC signature high-expressed genes reported in various studies[3] (Supplementary Fig. 1E). Additionally, we identified a rare cluster of Bgc cells that highly expressed the pre-germinal center (pre-GC) B cell signature reported previously[21] (Fig. 2C). These cells showed increased Myc pathway activity (Fig. 1C and Supplementary Fig. 1E), essential for germinal center initiation[22]. Given the high expression of genes related to C11 cells' class switch recombination (CSR) (Supplementary Fig. 1D), we classified C1_GC as pre-GC cells. Also, C3_Bm_TCL1A was identified as an intermediate state between Bm and Bn cells, characterized by the simultaneous high expression of markers from both lineages. For the Bn cells, we characterized four distinct subsets based on differential gene expression: C1_Bn_NFKB1, C2_Bn_AUTS2, C3_Bn_NR4A2, and C4_Bn_CD200. Notably, two of these populations, C3_Bn_NR4A2 and C4_Bn_CD200, exhibited high expression of the pre-GC B cell signature, as well as response to IFN-γ and antigen processing and presentation pathways (Fig. 1C and Supplementary Fig. 2A, D, and G). This result suggests that these two B cell subpopulations may play an important role in the immune response to breast cancer. All PC subsets exhibited elevated expression of well-known PC makers and transcription factors linked to PC differentiation, such as PRDM1, IRF4, and XBP1 (Supplementary Fig. 1E). We classified the PCs into nine distinct subsets based on DEGs. Among these, C1, C2, and C3 PC subsets retained the expression of major histocompatibility complex (MHC)-II genes (Fig. 3C), suggesting a transitional state prior to full maturation as PCs[23]. Notably, CD37 and STAT3 were still moderately expressed in C5_PC and C6_PC cells (Supplementary Fig. 1E), indicating a long-lived phase of PC differentiation[24].

In summary, we created a comprehensive transcriptome map of B cells, offering an in-depth characterization of fine-grained subsets. A combined analysis of tissue distribution, transcriptional, and sequence characteristics highlighted potentially tumor-reactive B cells originating from various tissue sources. We subsequently analyzed the abundance and cellular composition of B lineage cells in BRCA, matched normal tissues, metastatic lymph nodes, and peripheral blood (Fig. 1D). TABs contained more PCs than Bn cells compared to non-tumor tissues, while B cells in the blood were primarily enriched in Bn cells. Through analysis of BCR-seq data, we identified distinct isotype distribution patterns across major B cell lineages (Fig. 1E). The Bn cluster was primarily associated with IgD and IgM isotypes, the PC cluster displayed a significant enrichment of IgG and IgA isotypes, while Bgc and Bm clusters exhibited a mix of different isotypes. Next, we quantified the somatic hypermutation (SHM) level of each cluster, defined as the point mutation rate in the immunoglobulin (Ig) variable region, and categorized them into three tiers: high SHM (>10%), medium SHM (5–10%), and low SHM (mutation rate <5%). Bn cells predominantly exhibited low SHM levels in their BCRs, whereas Bgc cells, Bm cells, and ASCs showed medium to high SHM levels, consistent with their progressive maturation stages (Fig. 1E). To further investigate, we divided Bm cells, Bgc cells, and ASCs into two groups based on median SHM levels, finding that the marker CD27, a marker of B cell maturation, was significantly upregulated in the high-SHM group, while IGHD and IGHM were more highly expressed in the low-SHM group. Together, our data provide a valuable resource for studying the transcriptional phenotypes and clonal states of infiltrating B cells in human BRCA.

Identification of potential B cell subsets linked to immune responses in tumors

Using single-cell data, we aimed to identify key B cell subclusters that may contribute to the tumor immune response, analyzing them from three perspectives: clonal expansion, proliferation, and tumor enrichment. Through $R_{O/E}$ analysis[25], we uncovered substantial differences between tissue-infiltrating and circulating B cells. In the blood, PCs were notably less abundant compared to tissue, with a few B cell subset, such as C4_Bm_FGR, C4_Bn_CD200, C5_Bm_ISG15, and C2_Bm_NCF1, remaining primarily enriched (Fig. 2A). Interestingly, B cell compositional diversity in blood was lower than in ANTs or tumors, with tumor-associated B cells exhibiting the greatest diversity among the three (Supplementary Fig. 3C). Additionally,

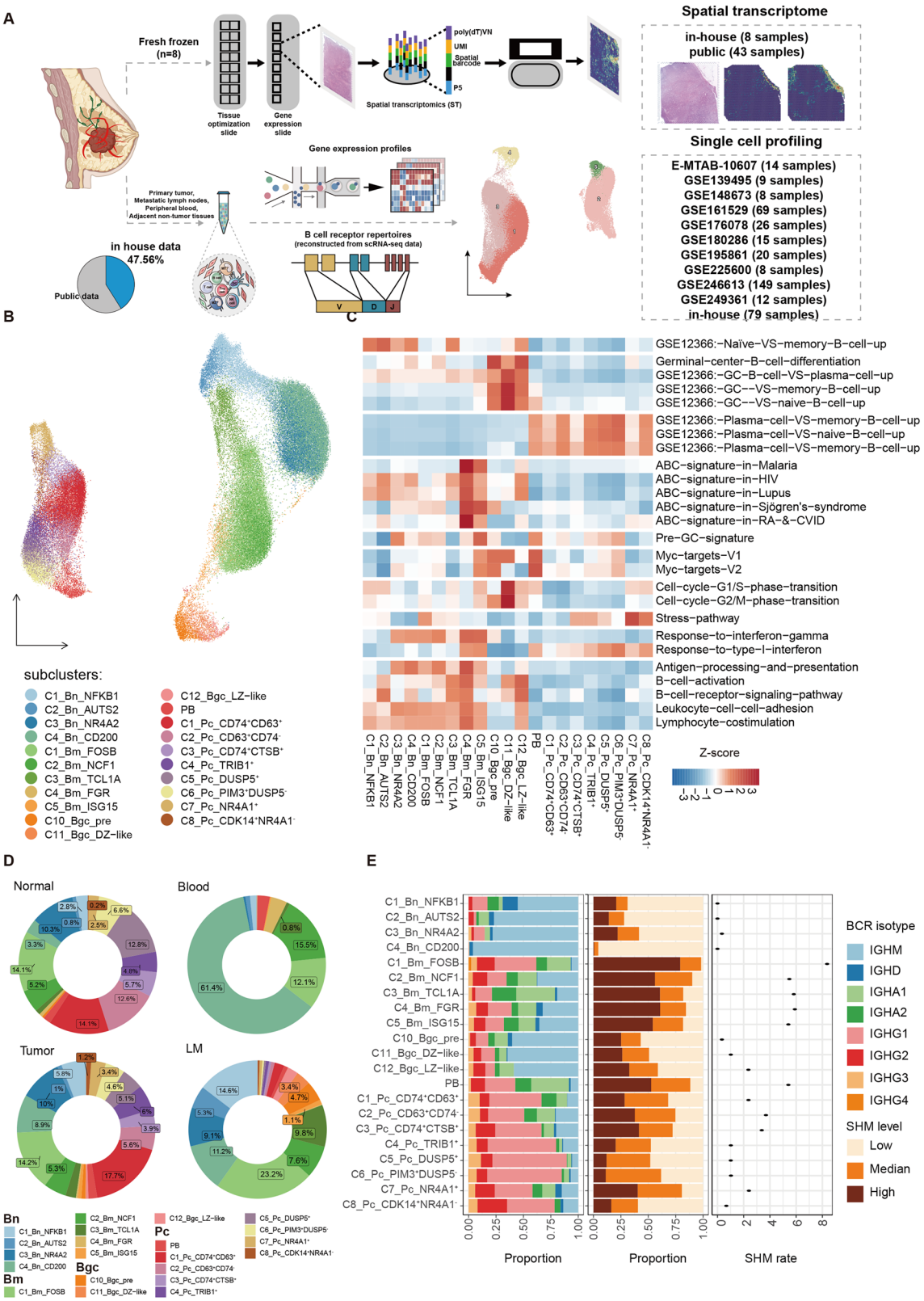

Fig. 1 | Breast-cancer single-cell profiling of B cells. A Schematic overview of the B cell atlas. **B** Uniform Manifold Approximation and Projection (UMAP) plots showing the major clusters and subsets of B cells. **C** Heatmap displaying gene signature expression across B cell subsets. **D** Donut charts showing the percentage of cells from different tissue origins. **E** Distribution of IgH isotype (left) and SHM levels (middle) across TAB subsets, with the median SHM rate shown for each subset (right).

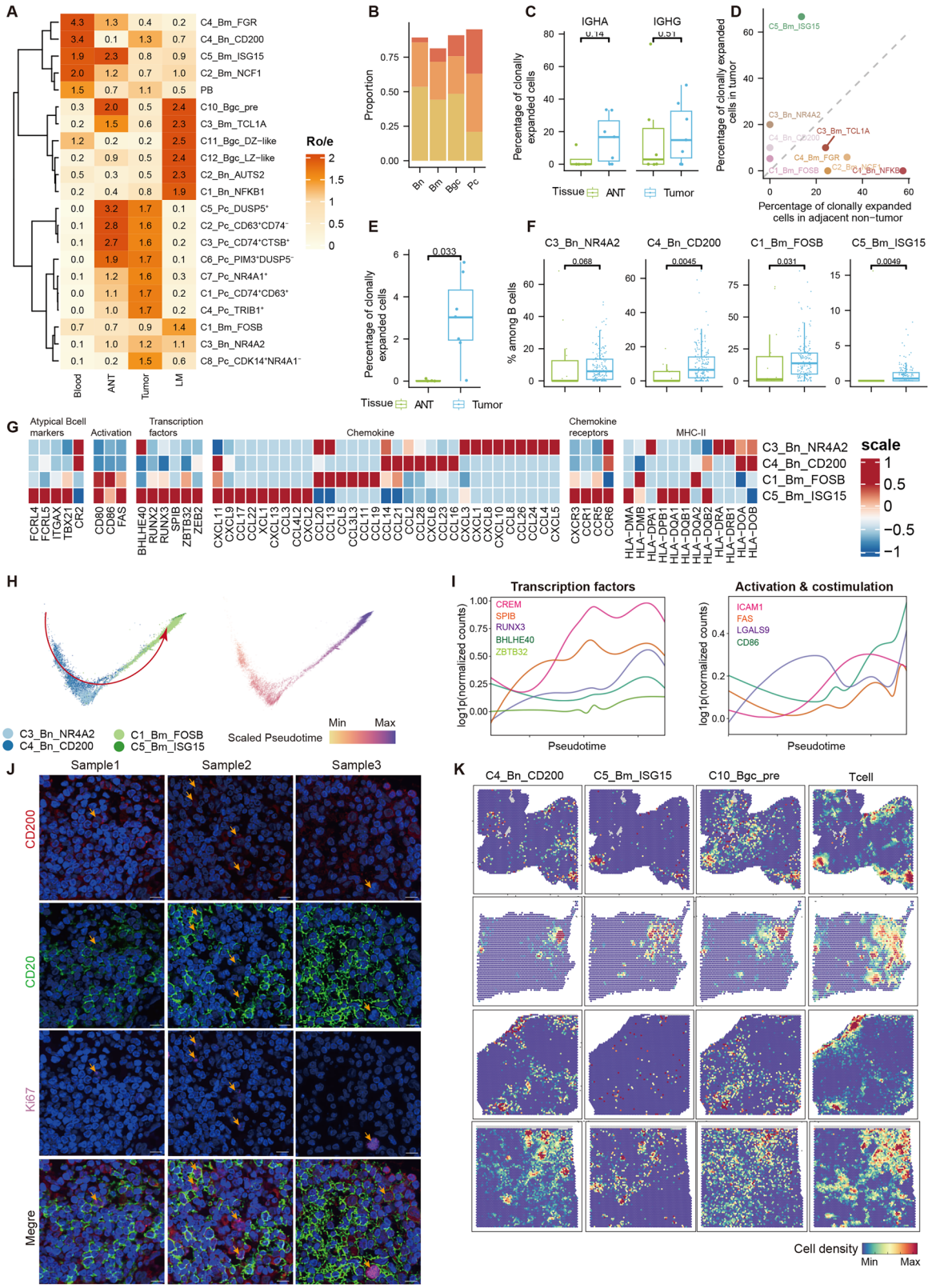

certain PCs (e.g., C5_PC, C2_PC, C3_PC, C6_PC) were enriched in ANTs, whereas subsets such as C3_Bn-NR4A2, C4_Bn_CD200, C7_PC, C1_PC, C4_PC, and C8_PC displayed a strong preference for tumors (Fig. 2A). Notably, C4_Bn_CD200 showed a high enrichment in both blood and tumors, while being sparse in ANTs, suggesting that C4_Bn_CD200 may migrate from the blood into the TME.

The clonal expansion and proliferation triggered by antigens are hallmark features of the B cell response[26]. Our analysis of the BCR repertoire revealed that tumor tissues contained a significantly higher proportion of B cell clones with sizes greater than five, indicating an active B cell immune response (Supplementary Fig. 3D). As anticipated, Bgc and PC lineages in tumors exhibited greater clonal expansion than Bm and Bn cells (Fig. 2B),

Fig. 2 | Identification of potential B cell subsets associated with immune responses in tumors. A Tissue preference of each B cell subset evaluated by the $R_{O/E}$ index. **B** Clonal expansion levels of major B cell lineages in tumors, with cells categorized by the clone size of their respective clones. **C** Boxplot comparing the percentage of clonally expanded cells (defined as cells from clonotypes with clone size >1) in IgA and IgG isotype PCs between tumors and ANTs. **D** Scatter plot showing the median percentage of clonally expanded cells in each Bn and Bm subset from tumors and ANTs. **E** Boxplot comparing the percentage of clonally expanded cells in C4_Bn_CD200 cells between tumors and ANTs. **F** Boxplots comparing the proportions of C3 and C4 Bn, and C1 and C5 Bm in total B cells between tumors and ANTs. Only treatment-naive samples with B cell counts >50 are shown. **G** Heatmap showing functional gene expression patterns in TAB subsets, with color indicating Z-score normalized expression. **H** Differentiation states estimated using diffusion maps. **I** Relationship between selected gene expression and pseudotime, with a 95% confidence interval. **J** Representative mIHC images of tumor samples showing the presence of $Ki67^+CD200^+$B cells (arrows). Scale bars, 50 μm. **K** Spatial feature plots displaying signatures of C4_Bn_CD200, C5_Bm_ISG15, C10_Bgc_pre, and T cells from ST data.

aligning with their involvement in the clonal expansion phases. In the PC lineage, we further compared different isotypes' clonal expansion capacities. Notably, IgA and IgG isotype PCs showed similar clonal expansion in ANTs, whereas IgG and IgA PCs from tumors displayed a trend toward higher clonal expansion compared to those in ANTs (Fig. 2C).

Relatively few Bn and Bm cells underwent clonal expansion (Fig. 2B), yet the C3_Bn_NR4A2, C4_Bn_CD200, C1_Bm_FOSB, and C5_Bm_ISG15 subsets displayed notably higher clonal expansion levels within tumors (Fig. 2D and Supplementary Fig. 3E). In addition, C4_Bn_CD200 cells derived from tumors exhibited more extensive expansion compared to those from ANTs (Fig. 2E), suggesting that tumor-specific stimuli may be driving their clonal expansion. The proportion of C4_Bn_CD200 cells within Bn cells was also significantly higher in tumor tissues than in ANTs (Fig. 2F). Given the high enrichment of tumor-infiltrating C3_Bn_NR4A2, C4_Bn_CD200, C1_Bm_FOSB, and C5_Bm_ISG15 subsets in both proportion and clonal levels within tumors, we designated these subsets as tumor-associated B cells (TABs). Next, we investigated the molecular characteristics of TABs within tumors. Notably, these cells demonstrated heightened activity across multiple pathways related to BCR signaling and B cell activation, along with a distinct chemokine expression profile (Fig. 2G). Similarly, compared to Bm cells enriched in other tissues, the C5_Bm_ISG15 subset, the terminal differentiation subgroup of TABs, exhibited increased expression of B cell activation markers such as FAS (encoding CD95), CD80, and CD86 (Fig. 2G).

Additionally, the transcription factors SPIB and BHLHE40, known for regulating BCR signaling and influencing B cell activation[27,28], were highly expressed in C5_Bm_ISG15. We also observed elevated expression of various cytokine receptors in C5_Bm_ISG15, including CXCR3, CCR1, and CCR1 (Fig. 2G), which are involved in inflammatory signaling responses[29–31]. We analyzed the developmental dynamics of tTAB by examining their lineage relationships with other B cell subsets. Specifically, we focused on four subsets, C3_Bn_NR4A2, C4_Bn_CD200, C1_Bm_FOSB, and C5_Bm_ISG15, and employed diffusion maps[32] to explore their transition trajectories. A directional flow was observed, beginning from C4_Bn and C3_Bn cells, progressing towards C5_Bm cells. Monocle3, as another single-cell fate-mapping algorithm[33], predicted $ISG15^+$Bm cells as the terminal state. Correlating pseudotime with gene expression profiles, we found that an increase in pseudotime was associated with a gradual ABC marker genes upregulation, T cell co-stimulatory genes, and inflammatory cytokine receptors (Fig. 2H, I). Together, our findings indicate the differentiation and activation states of TABs. Furthermore, multiplex immunofluorescence (mIF) staining has confirmed the presence of $Ki67^+CD200^+$Bn cells in tumor samples from thirty immunotherapy patients (Fig. 2J). These observations highlight $CD200^+$Bn cells' proliferative capacity, suggesting their sustained presence in the TME. We analyzed 51 ST datasets, encompassing 88,901 spots from both in-house and public sources, to compute correlations among TABs, Bgc, and T cells. As shown in Fig. 2K, C4_Bn_CD200, C5_Bm_ISG15, Bgc, and T cells were highly enriched. Additionally, C4_Bn showed significant co-localization with various TLS-related genes, suggesting that C4_Bn_CD200 is an integral component of TLS in BRCA, playing a critical role in the tumor immune response. In summary, these analyses underscore that specific B cell subclusters, including $CD200^+$Bn cells and $ISG15^+$Bm cells, may actively participate in tumor-associated immune responses.

Heterogeneity of tumor-infiltrating antibody-secreting cells

PCs are terminally differentiated B cells that fulfill their effector role by producing antibodies and expressing markers such as CD138, CD38, BLIMP-1, and IRF4. They are key components of the TME and are widely distributed across solid tumors[25]. However, the heterogeneity of PC subgroups in BRCA remains unclear. To investigate this, we corrected batch effects using fastMNN (Supplementary Fig. 4A), similar to our approach for other cell types. Subset of the PC compartment (excluding plasmablasts (PBs)) indicated eight distinct PC subsets, each with unique gene signatures and tissue distributions (Fig. 3A, B). Among these, C7_PC, C1_PC, and C4_PC were predominantly found in tumors, while C5_PC, C2_PC, C3_PC, and C6_PC accumulated in ANTs. C8_PC was prevalent in both lymph node metastases and tumors, while no prominent PC populations were detected in peripheral blood (Supplementary Fig. 4B). We then explored the molecular characteristics of tumor-associated PCs. Notably, among these subclusters, C1, C2, and C3 PCs retained the expression of MHC-II genes, suggesting a transitional state before full maturation as PCs. Furthermore, C7, C1, and C3 PCs exhibited significant chemokine expression, indicating their potential involvement in the tumor immune response (Fig. 3C). Additionally, compared to ANTs, the proportions of C1_PC, C8_PC, and PBs were significantly elevated in tumor tissues (Fig. 3D and Supplementary Fig. 4B).

Our next objective was to conduct a thorough analysis of PC differentiation states. To achieve this, we reconstructed the developmental trajectory of PCs using diffusion maps and Monocle3 (Fig. 3E). Pseudotime analysis identified multiple states of PC differentiation, including long- and short-lived PCs. Long-lived PCs showed high expression of IKZF3 (Aiolos), STAT3, and CD37 (Fig. 3F), aligning with their roles in supporting PC longevity[34–36]. Correlating pseudotime with gene expression profiles showed that increasing pseudotime was associated with a gradual upregulation of IGHA1 and IGHA2, suggesting that long-lived PCs exhibit higher levels of IgA antibody secretion (Fig. 3G).

Isotype shift from IgA to IgG in intratumoral PC response

Next, we examined the PC lineage's features, focusing on the tumor-enriched PCs identified previously. PCs exhibited high variability across different cancer types, largely due to cancer-type-specific expression preferences for Ig genes[3]. We compared the isotype composition of PCs between ANTs and tumors and found that IgG1 was the most frequent isotype in PCs from tumor samples, showing a significant increase compared to ANTs, while other IgG isotypes exhibited minimal changes (Fig. 3H). Next, we analyzed BCR repertoire overlap between upstream and downstream isotypes, based on the genomic order (5′ to 3′) of Ig subclass coding genes (e.g., IgG1, IgG2, IgG4, IgG3, IgA1, and IgA2). Consistently, we found a higher proportion of upstream antibody isotypes (IgG3 and IgM/D) sharing clonotypes with IgG1 in tumors (Fig. 3I). This suggests that isotype switching to IgG1 may occur more frequently in BRCA. Additionally, IgA1 and IgA2 isotypes were significantly reduced in tumors compared to ANTs (Fig. 3H, I). In breast tumors, IgA^+ cells were mainly

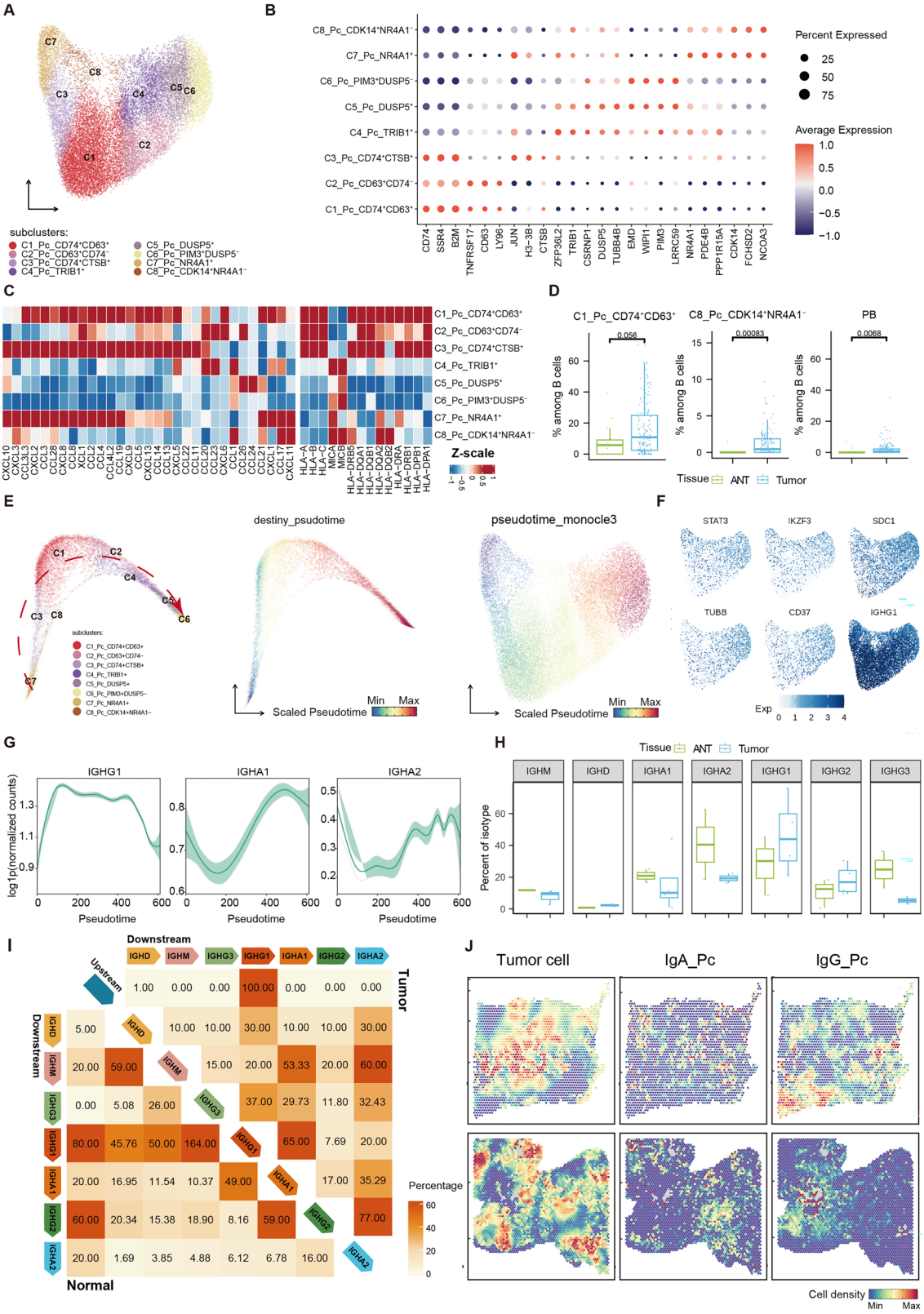

localized to regions of normal tissue adjacent to the tumor, whereas IgG$^+$ cells were primarily concentrated within the tumor region itself (Fig. 3J). Finally, we investigated interactions mediated by antibodies' fragment crystallizable (Fc) regions produced by IgA and IgG PCs, guided by Fc receptors' expression in different immune cell subtypes within the TME (Supplementary Fig. 3F). Compared to the selectively IgA-binding Fc alpha receptors (FcαRs), Fc gamma receptors (FcγRs), which bind IgG, were highly expressed across several subtypes of cytotoxic natural killer (NK) cells, DC_CD1C dendritic cells, and macrophages. Additionally, neutrophils expressed both FcαRs and FcγRs. In summary, PCs within the tumor showed an isotype shift from IgA to IgG dominance, although IgA PCs remained present at a moderate level.

Fig. 3 | Heterogeneity of tumor-infiltrating antibody-secreting cells. A Subset annotation of PC clusters. **B** Dot plot showing marker gene expression in PC subsets. Colors represent the maximum normalized mean expression of marker genes, and dot size indicates the percentage of cells expressing these genes. **C** Heatmap showing functional gene expression patterns in TAB subsets, with color indicating Z-score normalized expression. **D** Boxplots comparing the proportions of C1 and C8 PCs, and plasmablasts (PB) within total B cells between tumors and ANTs. Only treatment-naive samples with B cell counts >50 are included. **E** Differentiation states estimated using diffusion maps and Monocle3. **F** UMAP plot from (**A**), with cells color-coded based on the expression levels of four markers associated with long-lived PCs. **G** Relationship between selected gene expression and pseudotime, with a 95% confidence interval. **H** Boxplots comparing the composition of PC IgH isotypes between tumors and ANTs. **I** BCR repertoire overlap across B cells with different IgH isotypes in tumors (top right) and ANTs (bottom left). Heatmap showing the proportions of BCR clonotypes from each upstream isotype (rows) that are shared with each downstream isotype (columns). **J** Spatial feature plots displaying signatures of IgA and IgG PCs from spatial transcriptomics data.

High CD200$^+$B cell signature predicts better survival and response to immunotherapy

To evaluate the clinical relevance of TABs, we first used our scRNA-seq data to construct cell-type-specific gene signatures for the major TAB subgroups as previously described[6], confirming the reliability of these signatures in deconvolution analysis. Using both TCGA and in-house bulk data, we examined the association between B cell subgroup signatures and overall survival in cancer patients, adjusting for total B cell abundance. Notably, consistent results from TCGA and in-house data showed that B cell subgroups were associated with cancer type and patient prognosis (Supplementary Fig. 5A). Patients with relatively high expression of the CD200$^+$Bn marker were associated with longer survival times. In contrast, another B cell subset, C1_Bn_NFKB1 and C11_Bgc_DZ-like, was associated with poor survival, though this trend was not consistently observed in TCGA-BRCA data (Fig. 4A). We further evaluated the predictive power of the C4_Bn_CD200 signature for immunotherapy response by calculating AUC values across six immunotherapy cohorts, including non-small cell lung cancer (NSCLC) (GSE135222, GSE166449, GSE126044), metastatic melanoma (GSE168204, GSE35640), and metastatic or recurrent colorectal cancer (GSE19862) (Fig. 4B). The C4_Bn_CD200 signature demonstrated a higher average AUC value of 0.77, suggesting that it may act as a promising predictive marker for immunotherapy efficacy.

In subsequent analyses of immunotherapy or neoadjuvant treatment cohorts (metastatic melanoma [GSE168204, GSE91061, GSE35640], NSCLC [GSE166449, GSE135222, GSE126044], and breast cancer [GSE192341, GSE25065]), therapy responders (R) displayed higher C4_Bn_CD200 signature scores compared to non-responders (NR) (Fig. 4C). Additionally, Kaplan–Meier analysis showed that the C4_Bn_CD200 signature in the TCGA-BRCA cohort was associated with better overall survival (OS) ($P = 0.00015$, Fig. 4D), and this association was also observed in in-house cohorts ($P = 0.027$, Fig. 4E). Moreover, in several immunotherapy datasets, C4_Bn_CD200 infiltration levels were significantly associated with patient prognosis. In the bladder cancer dataset IMvigor210, higher C4_Bn_CD200 infiltration was correlated with better prognosis in immunotherapy patients ($P = 0.013$, Fig. 4F). A similar trend, though not statistically significant, were observed in the NSCLC dataset GSE135222 ($P > 0.05$, Fig. 4G) and melanoma dataset GSE78220 ($P > 0.05$, Fig. 4H), likely due to the limited sample size. Interestingly, in the clear cell renal cell carcinoma (ccRCC) CheckMate cohort, C4_Bn_CD200 infiltration was inversely correlated with a favorable prognosis in immunotherapy patients ($P = 0.021$, Fig. 4I), indicating that C4_Bn_CD200 may play distinct roles in immune responses across different cancer types. These findings highlight the importance of further investigating the function and mechanisms of C4_Bn_CD200 to enhance our understanding of its role in tumor immunity. Overall, these data suggest that C4_Bn_CD200 levels have the potential to serve as a unique prognostic factor in clinical immunotherapy.

CD200$^+$ TABs play a crucial role in sustaining anti-tumor immune responses and effectively suppress tumor growth

To understand the role of CD200$^+$TABs in anti-tumor immunotherapy response, we characterized the phenotype of CD200$^+$TABs and investigated their distribution in blood, spleen, normal breast tissue, and tumors in 4T1 tumor-bearing mice ($n = 6$ mice per group) (Supplementary Fig. 8). CD200$^+$ TABs were relatively abundant in blood and tumor tissue, while their presence in normal tissue was significantly lower. Consistent with findings from human single-cell data, this suggests that CD200+TABs may represent a subset active within the TME of 4T1 tumor-bearing mice. Based on the strong evidence, we further explored whether targeting CD200+CD19+B cells in BRCA could reshape the immunosuppressive TME in vivo. To simulate the relevant B cells in human BRCA, we isolated CD200+CD19+B cells and CD200$^-$CD19+B cells from the spleen and injected them into mice through the tail vein (Fig. 5A). In addition, all mice underwent B cell depletion prior to treatment to assess the impact of CD200$^+$CD19$^+$B cells on tumor progression. Interestingly, the adoptive transfer of CD200+CD19+B cells, in contrast to CD200$^-$CD19+B cells, significantly inhibited 4T1 tumor growth (Fig. 5B–D). Similarly, CD200$^+$CD19$^+$B cell adoptive transfer markedly suppressed E0771 tumor burden compared to CD200$^-$CD19$^+$B cells, correlating with enhanced anti-tumor immunity (Fig. 6E, F). Consistent with our expectations, adoptive transfer of CD200$^+$CD19$^+$B cells, in contrast to CD200$^-$CD19+B cells, significantly elevated the secretion levels of IFN-γ and GZMB by cytotoxic T cells within the tumor (Fig. 6G, H). Additionally, PD-1 expression on CD8$^+$T cells increased notably, suggesting that CD200$^+$CD19$^+$B cell transfer may effectively enhance the response to anti-PD-1/PD-L1 therapy. These findings indicate that CD200+, CD19+, and CD200$^-$CD19+B cells play distinct roles within the TME.

Additionally, we explored the impact of anti-CD200 treatment on tumor growth. To assess the efficacy of CD200$^+$TAB depletion through antibody treatment, we administered anti-CD200 antibodies to tumor-bearing mice without other treatments to deplete CD200$^+$TABs ($n = 6$ mice per group). Previous studies have shown that anti-CD200 antibodies not only reduce CD200$^+$TABs but also lead to a reduction of approximately 25% in CD4$^+$T cells and 50% in B cells[37]. As shown, CD200 inhibitor treatment did not significantly inhibit tumor growth compared to the control antibody treatment group (Fig. 5K–N). This lack of effect may be due to the simultaneous reduction of T and B cells by the anti-CD200 antibody, thereby having minimal impact on tumor growth. In summary, these results suggest that B cell subgroups display functional heterogeneity, with CD200$^+$CD19$^+$B cells potentially possessing anti-tumor immune properties compared to CD200$^-$CD19+B cells.

CD200$^+$TABs are required for efficacious anti-PD-1 therapy

To investigate whether CD200$^+$TABs could enhance the effectiveness of immunotherapy, we first examined the infiltration levels of CD200$^+$TABs in the tumor regions of mice before and after immunotherapy. In the breast cancer (4T1) mouse model ($n = 6$ mice per group), we observed a rise in CD200$^+$B cells following anti-PD-1 treatment, relative to control mice treated with a non-therapeutic antibody (Fig. 6A). We further assessed the proportions of naive and memory cells within the CD200$^+$B cell population in tumors and noted a trend toward an increase in CD200+Bn cells, although this difference was not statistically significant (Fig. 6A). To assess if CD200$^+$TABs are essential for effective anti-PD-1 therapy, we eliminated B cells in 4T1 tumor-bearing mice that did not receive anti-PD-1 treatment using anti-CD19 antibodies ($n = 6$ mice per group). These mice were later treated with PD-1 blockade and received CD200$^+$Bn cell transfers as indicated in Fig. 6B. Both anti-PD-1 treatment alone and CD200$^+$Bn cell transfer alone showed modest effects in slowing tumor growth. As expected,

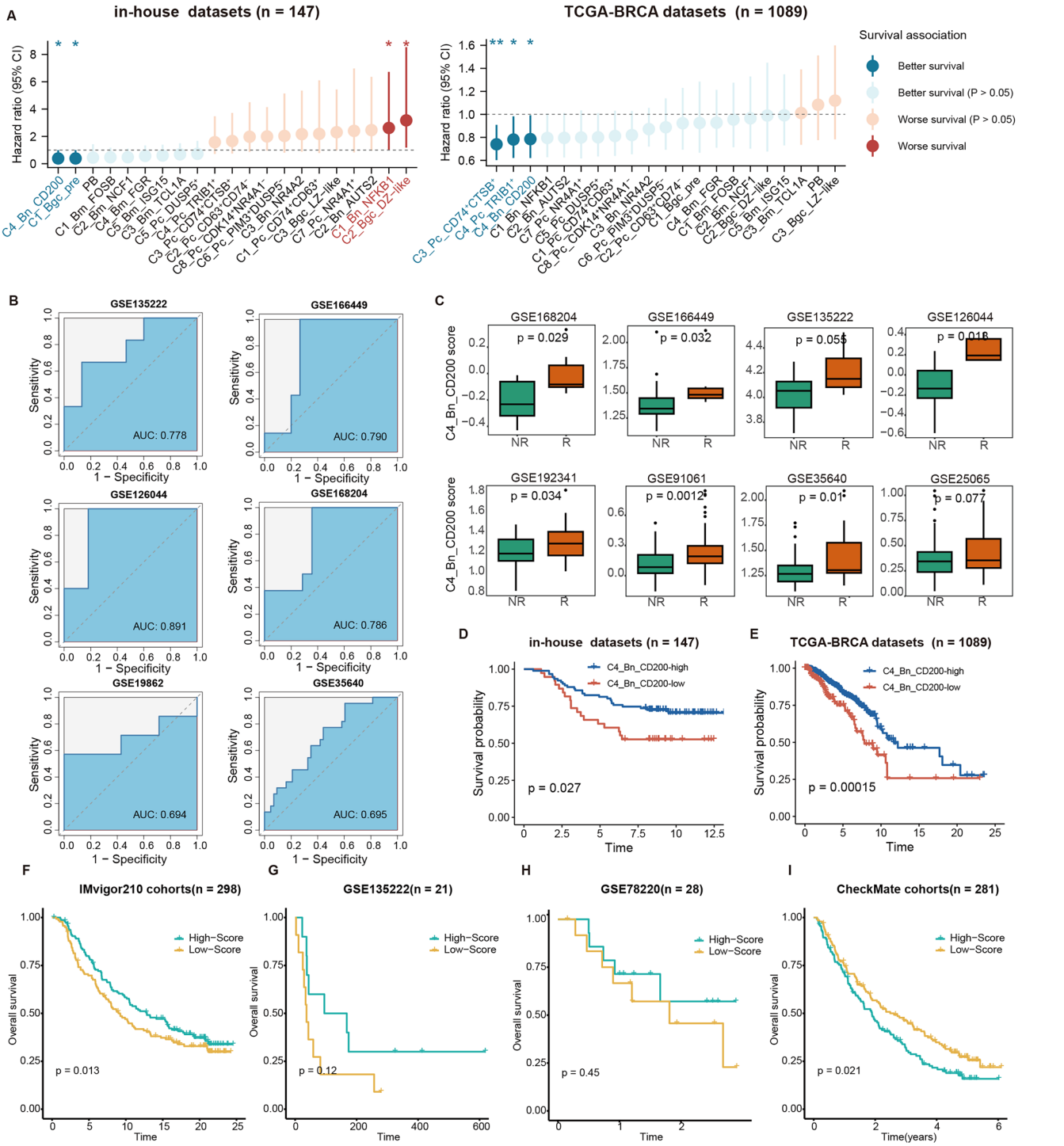

Fig. 4 | C4_Bn_CD200 TAB signature in BRCA predicts improved survival and response to immunotherapy. A Prognostic associations of each B cell subset signature, shown for in-house datasets (left) and TCGA-BRCA datasets (right). **B** ROC curves for the CD200$^+$TAB gene signature predicting the benefits of fluorouracil-based ACT in non-small cell lung cancer (GSE135222), breast cancer (GSE166449), gastric cancer (GSE126044), metastatic melanoma (GSE168204), colorectal cancer (GSE19862), and breast cancer (GSE35640). **C** Distribution of the CD200$^+$TAB gene signature between responders and non-responders to immunotherapy or neoadjuvant therapy in multiple datasets: metastatic melanoma (GSE168204, $n = 27$, $P = 0.029$; GSE91061, $n = 109$, $P = 0.0012$; GSE35640, $n = 65$, $P = 0.01$), non-small cell lung cancer (GSE166449, $n = 22$, $P = 0.032$; GSE135222, $n = 27$, $P = 0.055$; GSE126044, $n = 16$, $P = 0.0018$), and breast cancer (GSE192341, $n = 87$, $P = 0.034$; GSE25065, $n = 198$, $P = 0.072$). Statistical test: two-sided t-test. Kaplan–Meier curves showing differences in OS probability between patients with high vs. low levels of the CD200$^+$TAB gene signature in in-house (**D**) and TCGA-BRCA (**E**) cohorts. **F–I** Predictive value of CD200$^+$TAB infiltration for survival in patients receiving immune checkpoint blockade (ICB) treatment, as shown across individual datasets.

the combination of CD200$^+$Bn cell transfer with anti-PD-1 therapy significantly enhanced the efficacy of tumor control in breast cancer (Fig. 6C–E). A similar synergistic effect was observed in E0771 tumors, a spontaneous breast cancer model derived from C57BL/6 mice (Fig. 6F, G). To further assess the impact of CD200$^+$TAB transfer on the TME, we used flow cytometry and observed that the combination of CD200$^+$TAB transfer with immunotherapy notably increased the proportion of effector CD8+T cells (Fig. 6H–L). In summary, our findings suggest that CD200$^+$TABs are

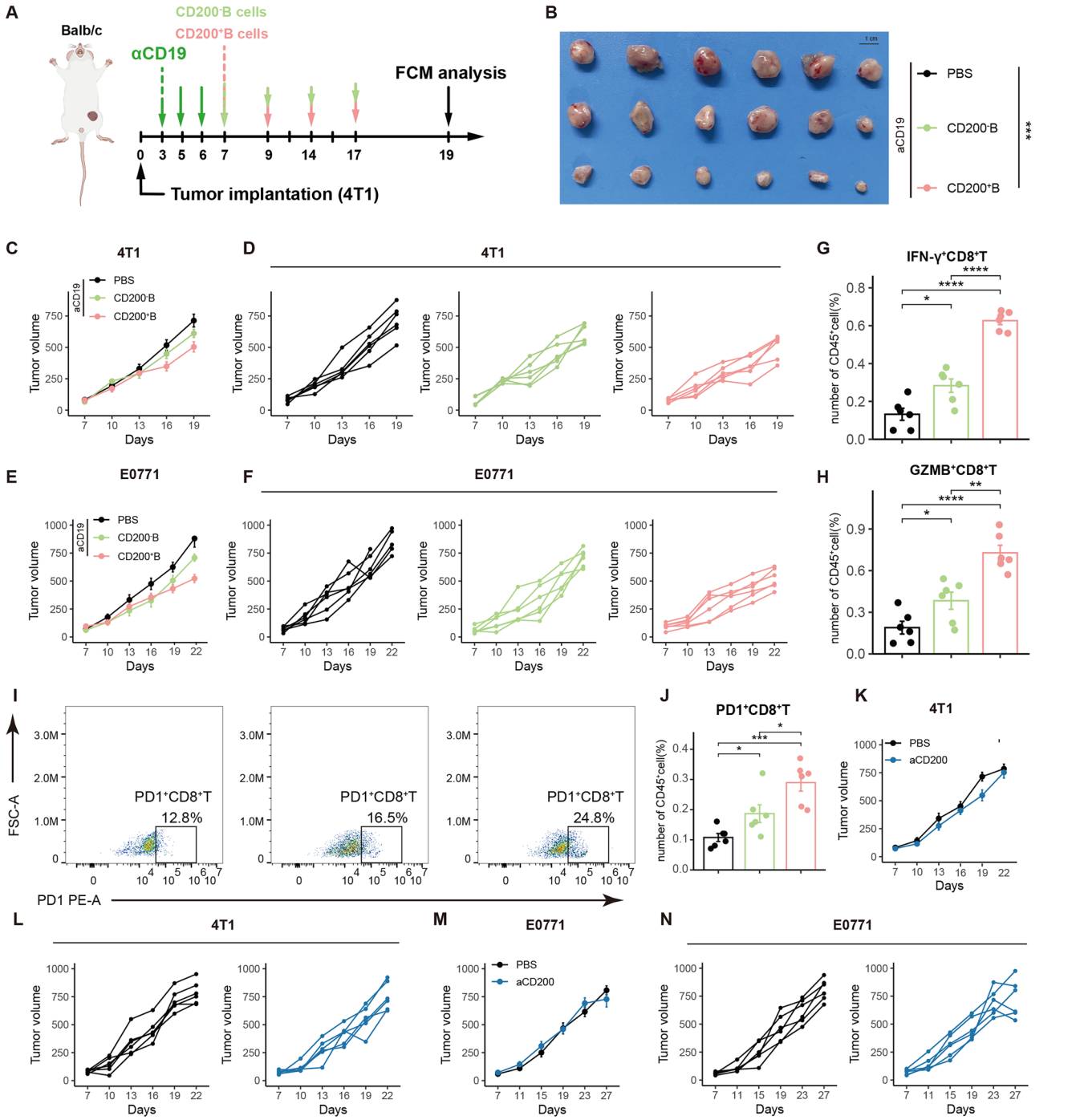

Fig. 5 | Co-inoculation of CD200$^+$ TABs with tumor cells effectively controls tumor growth. A–D 4T1 cells were subcutaneously inoculated into the right flanks of mice. CD200$^+$ or CD200$^-$TABs isolated from the spleen were then injected via the tail vein. Shown are the experimental schedule (**A**), representative tumor images (**B**), tumor growth curves (**C**), and individual tumor growth curves (**D**) ($n = 6$ mice per group, $n = 3$). Tumor growth curves (**E**) and individual tumor growth curves (**F**) for E0771 tumors ($n = 6$ mice per group, $n = 3$). **G–J** Flow cytometric analysis of GZMB$^+$CD8$^+$T cells, IFN-γ+CD8+T cells, and PD-1+CD8+T cells in tumors treated as described in (**A**). Representative flow cytometry images (**I**) and quantification of GZMB$^+$ (**G**), IFN-γ$^+$ (**H**), and PD-1$^+$ (**J**) CD8$^+$ T cells are shown. **K–N** Effect of CD200 inhibitor treatment on tumor growth. Shown are tumor growth curves (**K**, **M**) and individual tumor growth curves (**L**, **N**).

essential for the efficacy of anti-PD-1 therapy, warranting further investigation into the role of CD200$^+$TABs in enhancing immunotherapy outcomes.

Discussion

ScRNA-seq has become a valuable tool for investigating the complex TME of BRCA. Both our group and others have revealed that the local TME harbors immune cells with distinct phenotypes and intricate intercellular interactions[6,38,39]. However, immunobiological studies of BRCA and other solid tumors have primarily focused on T cells, with relatively limited characterization of TABs. Previous single-cell studies largely classified TABs into B cells and PCs, considering each as a homogeneous subset. In this study, we leveraged our unique scRNA-seq and scBCR-seq datasets, derived from tumor tissues, metastatic lymph nodes, peripheral blood samples, and matched normal tissues collected from BRCA patients undergoing surgery. By integrating these data with multiple published single-cell datasets, we

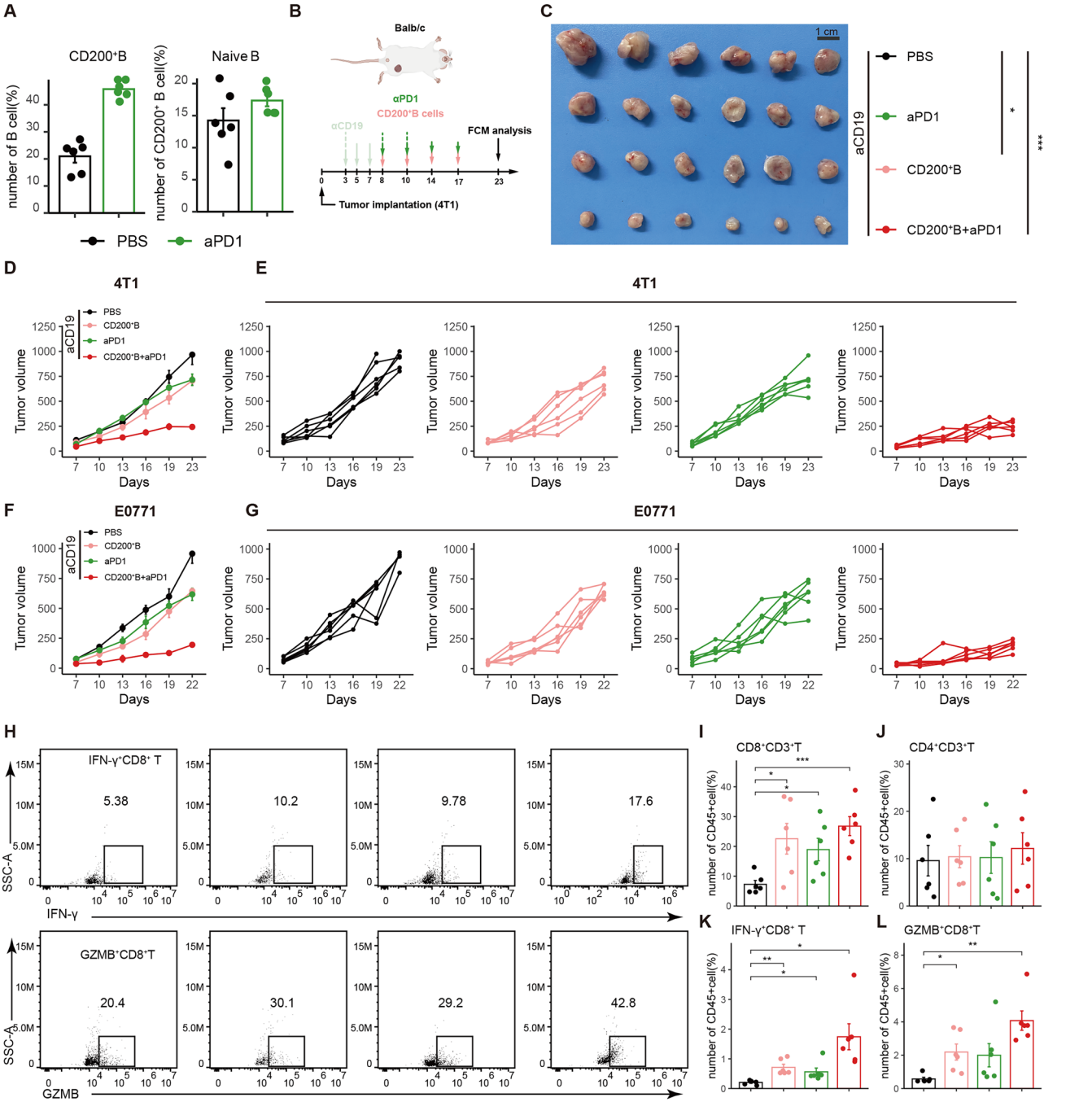

Fig. 6 | CD200$^+$TABs are essential for effective PD-1 blockade therapy. A, B 4T1 cells were subcutaneously inoculated into the right flanks of mice. Anti-PD-1 (α-PD-1) or control IgG2b (Ctrl) was administered intraperitoneally. Tumors were harvested on day 16 post-inoculation, and flow cytometry was used to analyze CD200$^+$B cells within TAB cells (**A**) and naive B cells among CD200$^+$B cells (**B**) ($n = 6$ mice per group, $n = 3$). **C–G** 4T1 or E0771 cells were subcutaneously inoculated into the right flanks of mice. Anti-PD-L1 or control IgG2b was administered intraperitoneally, and anti-CD19 (αCD19) or control IgG2a was injected via the tail vein. CD200$^+$B cells were also injected via the tail vein. Shown are the experimental schedule (**B**), overall tumor growth curves (**D**, **F**), individual tumor growth curves (**E**, **G**), and representative images (**C**) taken on day 16 post-tumor challenge. **H–L** Flow cytometric analysis of CD8$^+$CD3$^+$T cells, CD4$^+$CD3$^+$T cells, IFN-γ$^+$CD8$^+$T cells, and GZMB$^+$CD8$^+$T cells in tumors treated as described in (**A**). Representative flow cytometry images (**H**) and quantification (**I–L**) are shown.

constructed a large-scale transcriptional atlas of B cells. These in-depth single-cell maps of breast cancer-associated B cells provide a systematic characterization of TAB subsets, including their clonal states, spatial distribution patterns, and developmental dynamics, all at the single-cell level.

We confirmed extensive remodeling within the TME of BRCA, characterized by a notable increase in the proportion of memory B cells, particularly more differentiated PCs. Our analysis suggests that various microenvironmental factors may contribute to alterations in the TAB landscape within BRCA. Firstly, our previous studies identified a marked increase in CCL19 expression in CAFs, which aligns with the high enrichment of Bgc and T cells in BRCA, given CCL19's critical role in promoting TLS formation in breast cancer. Our data also facilitate the identification of key transitional subclusters within the intratumoral B cell differentiation pathway, like plasmablasts and pre-GC B cells. However, the presence of LZ/DZ-like Bgc cells was not significantly associated with better prognosis at a pan-cancer level. Since Bgc cells are rare and typically found only in partially mature TLSs within tumors, their impact on overall expression levels across samples is likely limited.

Interestingly, we discovered a tumor-enriched CD200$^+$Bn subcluster, which may contribute to antigen presentation during tumor-associated immune responses, suggesting a potential role for TABs in this process. Additionally, we identified two tumor-associated Bm subsets, C1_Bm_FOSB and C5_Bm_ISG15, which share gene characteristics with previously reported ABCs and memory-related B cells[19]. Compared to other tissue-enriched subsets, the tumor-enriched C3_Bn, C4_Bn, C1_Bm, and C5_Bm subsets exhibited higher levels of clonal expansion and proliferative capacity, and highly activated transcriptional states within tumors, thus termed TABs. Notably, the differentiation trajectory from C4_Bn_CD200 to C5_Bm_ISG15 is unique to tumors. Spatially, TAB-related subsets also showed substantial overlap with TLS structures, implying that C4_Bn_CD200 and C5_Bm_ISG15 may play key roles in TLS formation and the initiation of anti-tumor immune responses. Further research is needed to explore the mechanisms underlying the anti-tumor potential of TABs and their potential application in clinical practice. Additionally, our analyses revealed a high abundance of IgG$^+$PCs in BRCA, which frequently co-existed with activated and proliferative CD8$^+$Tex, Tregs, macrophages, and CAFs, while showing a negative correlation with CTLs. This observation aligns with evidence validating the pro-tumorigenic and immunosuppressive role of IgG$^+$PCs[31], although further functional studies are required to clarify their precise roles in BRCA pathogenesis.

Our analysis highlights the unique clinical significance of the C4_Bn_CD200 subset, as the C4_Bn_CD200 signature identified in this study shows a strong association with patient survival across various BRCA cohorts and is notably linked to responses to immunotherapy. Our findings further highlight the potential of the C4_Bn_CD200 signature as a promising predictive biomarker for BRCA patients. Notably, B cells are associated with poor prognosis in renal cancer[10], and a high Bn_CD200 signature predicts adverse outcomes in patients undergoing immunotherapy. This may be due to limited Bn_CD200 infiltration in most renal cancer patients, potentially restricting its beneficial effects[40]. Finally, we validated in animal models that Bn_CD200 supports anti-tumor immune responses in mice and enhances the efficacy of immune checkpoint inhibitors.

Although scRNA-seq provides a reliable approach for whole-transcriptome analysis of TABs, there are also some limitations in our study. When attempting to identify rare TAB subsets, we found that IL10$^+$Bregs were still difficult to detect in single-cell analysis, possibly due to the low capture efficiency of interleukin transcripts in scRNA-seq. Another possible reason for the low abundance of Bregs is that their state is dynamic and highly influenced by environmental factors. Recently, an expert's viewpoint on this issue indicates that Bregs represent a phenotypic state rather than a fixed spectrum[41,42]. Breg cells, at different stages of B cell maturation and differentiation, such as early transitional B cells, Bm cells, and plasmablasts, can be identified[4]. Nevertheless, this study offers essential insights into the previously unexplored phenotypic diversity and functions of TABs in BRCA, establishing a valuable resource for identifying targets to develop urgently needed for early treatment of BRCA. It also underscores the clinical relevance of the CD200$^+$Bn subset within TABs.

Methods

Patient inclusion and sample collection

Cancer tissues, adjacent normal tissues, lymph node metastases, and blood samples were collected from 35 treatment-naïve cancer patients at Harbin Medical University Cancer Hospital. All participants provided written informed consent, and the study was conducted in compliance with Institutional Review Board-approved protocols of Harbin Medical University Cancer Hospital (IRB: KY2019-08). The research adhered to the principles outlined in the Declaration of Helsinki. Detailed information can be found in Supplementary Table 1.

ScRNA-seq and scBCR-seq. Matched cancer tissues, adjacent normal tissues (ANTs), and LN_Met tissues were enzymatically dissociated using either the Tumor Dissociation Kit or Collagenase IV, following the manufacturer's instructions. These cells were sequenced using 10x Chromium Single-Cell 5′ and V(D)J library construction (10x Genomics, USA), as per the manufacturer's guidelines. We applied CellRanger V7 for read alignment and gene-count matrix generation and BCR sequence assembly. Potential doublets were identified and removed using DoubletFinder (v2.0.3)[43].

Public data collection. Public scRNA-seq datasets were obtained from sources such as Gene Expression Omnibus (GEO) database (GSE139495[44], GSE148673[40], GSE161529[45], GSE176078[37], GSE180286[46], GSE195861[47], GSE225600[48], GSE246613[41]) and the ArrayExpress database (E-MTAB-10607[49]). Additional data, including BRCA samples, were collected from the Cancer Genome Atlas (TCGA) data portal. A study provided spatial transcriptome information for 56 samples[50], which included BRCA tumors, normal tissues, and leading tissues. The immunotherapy and neoadjuvant therapy data collection is shown in our previous article[5].

ScRNA-seq data processing and annotation. Seurat (V5.0.1) processed the UMI count matrix, removed doublets, and filtered out cells with >30% mitochondrial gene expression. Highly variable genes (HVG) were identified using *FindVariableFeatures*, and cells were integrated using *harmony* (V0.1.0). Cell types were annotated based on markers for various immune and stromal cell types (e.g., CD79A and CD79B for B cells, PECAM1, VWF and CD34 for endothelial cells, COL1A1, COL1A2 and DCN for fibroblasts, C1QB, CSF3R, CLEC9A, and CD1C for myeloid cells, MZB1 and IGHG1 for plasma cells, CD3D, KLRD1, KLRC1, and CD3E for T/NK cells).

B cell subclustering. To achieve subclustering of B cells and PCs, Seurat's shared nearest neighbor (SNN) method was applied, utilizing the *Louvain* algorithm to identify 21 distinct subclusters (Fig. 1B). Differentially expressed genes (DEGs) for each subcluster were determined through the *FindAllMarkers* function in Seurat. These subclusters were subsequently analyzed to assess enrichment for cancer or tissue types and for specific cell subtype identification.

Scoring cells using gene expression signatures. The signature sets of B cells were collected from studies under various chronic disease settings, such as malaria[19], HIV infection[51], systemic lupus erythematosus (SLE)[52], Sjögren's syndrome[53], rheumatoid arthritis (RA), and common variable immunodeficiency (CVID)[54]. The pre-GC signature and CSR-related gene set originated from a study of human tonsillar B cells[21]. Other gene signatures used to characterize B cells in Fig. 1C were required from the MSigDB database (R package msigdbr, version 7.5.1). All assembled signature sources are publicly accessible and can be downloaded from earlier published studies[3]. The AddModuleScore function of Seurat was applied with default parameters to score each signature in each B cell, and the mean score of all cells in each B cell subset was calculated.

Tissue distribution of B cell subsets. To quantify the tissue preference of each B cell subset, we calculated the ratio of observed to expected cell numbers ($R_{O/E}$) across different tissue types, including adjacent normal tissue and tumor samples. Expected cell counts for each stromal subset-tissue combination were obtained from the chi-squared (χ^2) test. Subsets with $R_{O/E} > 1$ were classified as enriched within a specific tissue type.

Spatial transcriptomics. The space ranger output files were processed using Seurat (V4.0.4), with sample information provided in Supplementary Table 1. Data normalization was conducted with Seurat's *SCTransform* function, followed by dimensionality reduction using *RunPCA*, and clustering of spatial transcriptomics (ST) spots using *FindNeighbors* and *FindClusters*. Cell-type scoring involved estimating

stromal cell subset compositions through the *runRCTD* function from the RCTD package.

Evaluation of CD200$^+$TAB in bulk RNA-seq data. We developed a C4_Bn_CD200 cell feature gene set to quantify C4_Bn_CD200 infiltration in bulk RNA-seq data, through an unsupervised, two-step approach: (i) The transcriptome of C4_Bn_CD200 cells was compared with that of non-C4_Bn_CD200 cells, with DEGs identified as the C4_Bn_CD200 feature gene set. (ii) The gene set's specificity across all tumor-infiltrating cells was validated through ssGSEA. An infiltration score for C4_Bn_CD200 was subsequently calculated for each bulk sample via ssGSEA.

Cell culture. The 4T1 and E0771 cell lines were acquired from the American Type Culture Collection (ATCC). 4T1 cells and all primary immune cells were cultured in RPMI 1640 medium, while other cell lines were maintained in DMEM. Both media were supplemented with 10% heat-inactivated fetal bovine serum (FBS; Gibco) and 1% penicillin-streptomycin antibiotics (100 U/mL; Gibco). Cells were incubated at 37 °C in a humidified atmosphere with 5% CO_2.

Mice. Female C57BL/6 and Balb/c mice (6-week-old) were purchased from Wuhan Shubeili Biology Science and Technology Co., Ltd. Mice were housed in a specific pathogen-free (SPF) facility under controlled environmental conditions with a 12-h light/dark cycle (lights on from 7:00 a.m. to 7:00 p.m.), ambient temperature 22 ± 2 °C, and relative humidity 50–60%. Animals had free access to standard laboratory chow and autoclaved water. Sample sizes were estimated based on prior experience. The study was reported in accordance with the ARRIVE guidelines (Animals in Research: Reporting In Vivo Experiments). Mice were anesthetized with 1% pentobarbital sodium before all operations. Ethical approval for all animal experiments was granted by the Institutional Animal Care and Use Committee of Huazhong University of Science and Technology (No. IACUC [2023] 3525).

Tumor model and treatment. For tumor experiments, tumor cells (5×10^5 4T1 or 1×10^6 E0771) were suspended in 100 μL of phosphate-buffered saline (PBS) and injected subcutaneously into the 4–5 pairs of breast pads of mice on day 0. On day 7 post-inoculation, once the tumor reached 50 mm^3, these mice were randomly divided into different groups ($n = 6–8$ per group). Adoptive B cell therapy involved twice-weekly tail vein injections of CD200$^+$CD19$^+$B cells, CD200$^-$CD19$^+$B cells, or PBS (1×10^6 cells/100 μL) for two weeks. For anti-CD200 therapy, anti-CD200 (200 μg; clone OX-90, Bio X Cell) or control immunoglobulin G2a (IgG2a; 200 μg; clone 2A3, Bio X Cell) was administered via tail vein injections on days 7, 9, 14, and 17 after tumor inoculation. PD-1 blockade involved intraperitoneal injections of anti-PD-1 (200 μg; Bio X Cell) or control IgG2b (200 μg; clone LTF-2, Bio X Cell) on days 8, 10, 14, and 17 post-tumor challenge. The endpoint criteria included the development of tumors with a maximum diameter of 1200 mm, onset of necrosis, or death of any mouse. Tumor volume (mm^3) was measured with calipers and calculated as $0.5 \times \text{length} \times \text{width}^2$. Investigators responsible for tumor measurement and data analysis were blinded to the group allocation until the completion of the study. All sample processing and histological evaluations were performed by independent researchers who were unaware of treatment assignments. At the conclusion of the experiment, all mice were anesthetized by isoflurane inhalation until deep anesthesia was achieved, followed by cervical dislocation, and tumor tissues were surgically excised for further analysis. All animal experiments adhered to protocols approved by the Research Ethics Committee.

In vivo depletion of B cells. Mice were treated intraperitoneally with anti-CD19 (clone 1D3; Ref: BE0150; 150 μg) one day prior to subcutaneous tumor cell implantation, with additional doses administered every three days. Mouse IgG2a (clone MOPC-173, BioLegend) served as the isotype control. l B cell depletion was confirmed by flow cytometry.

Flow cytometry. Freshly excised mouse tumors were stored at 4 °C in tissue storage solution and analyzed within 4 g. Tissues were digested to promote dissociation using a mixture of 20 mg/mL dispase II, 20 mg/mL hyaluronidase, and 20 mg/mL collagenase for 60 min at 37 °C with rotation. Following digestion, single-cell suspensions were obtained by passing the mixture through a 70 μm cell strainer, and red blood cells were lysed at room temperature for 5–10 min. For surface staining, single-cell suspensions were incubated with directly conjugated antibodies for 30 min at 4 °C in the dark. For intracellular staining, cells were initially stained for surface markers, then fixed and permeabilized using the Cytofix/Cytoperm kit (BD Biosciences), followed by staining of intracellular proteins. Data acquisition was performed on a CytoFLEX S Flow Cytometer (Beckman Coulter), and data analysis was conducted using CytExpert software (Beckman Coulter, Version 2.3).

Statistical analysis. Data were analyzed using R software (V4.3.1) and are presented as mean ± SEM from independent biological replicates. Comparisons between two groups were performed using Student's *t*-test. For multiple group comparisons, one-way or two-way analysis of variance (ANOVA) with Bonferroni correction was applied. Survival curves were evaluated using the log-rank (Mantel-Cox) test. Statistical significance was defined as follows: $P < 0.05$, $^*P < 0.01$, $^{**}P < 0.001$, $^{***}P < 0.0001$, with "ns" indicating no significant difference.

Data availability

Publicly available datasets were analyzed in this study. Public data used in this work can be acquired from the TCGA repository (http://cancergenome.nih.gov/) and Gene Expression Omnibus (GEO, https://www.ncbi.nlm.nih.gov/geo/). The raw data and processed data of single-cell RNA-sequencing data and spatial transcriptomic data have been deposited in the Gene Expression Omnibus (GEO) database under accession codes GSE167036 and GSE190811. All other raw data generated in this study are available upon request from the corresponding author.

Code availability

No new algorithms were developed for this article. All code generated for analysis is available from the authors upon request.

Received: 13 March 2025; Accepted: 10 February 2026;
Published online: 12 March 2026

References

1. Nie, M. et al. Targeting acetylcholine signaling modulates persistent drug tolerance in EGFR-mutant lung cancer and impedes tumor relapse. *J. Clin. Invest.* **132**, e160152 (2022).
2. Wherry, E. J. & Kurachi, M. Molecular and cellular insights into T cell exhaustion. *Nat. Rev. Immunol.* **15**, 486–499 (2015).
3. Yang, Y. et al. Pan-cancer single-cell dissection reveals phenotypically distinct B cell subtypes. *Cell* **187**, 4790–4811.e4722 (2024).
4. Sharonov, G. V., Serebrovskaya, E. O., Yuzhakova, D. V., Britanova, O. V. & Chudakov, D. M. B cells, plasma cells and antibody repertoires in the tumour microenvironment. *Nat. Rev. Immunol.* **20**, 294–307 (2020).
5. Mazor, R. D. et al. Tumor-reactive antibodies evolve from non-binding and autoreactive precursors. *Cell* **185**, 1208–1222.e1221 (2022).
6. Cai, X. et al. Re-analysis of single cell and spatial transcriptomics data reveals B cell landscape in gastric cancer microenvironment and its potential crosstalk with tumor cells for clinical prognosis. *J. Transl. Med.* **22**, 807 (2024).
7. Fridman, W. H. et al. B cells and tertiary lymphoid structures as determinants of tumour immune contexture and clinical outcome. *Nat. Rev. Clin. Oncol.* **19**, 441–457 (2022).

8. Meylan, M. et al. Tertiary lymphoid structures generate and propagate anti-tumor antibody-producing plasma cells in renal cell cancer. *Immunity* **55**, 527–541.e525 (2022).
9. Schumacher, T. N. & Thommen, D. S. Tertiary lymphoid structures in cancer. *Science* **375**, eabf9419 (2022).
10. Iglesia, M. D. et al. Genomic analysis of immune cell infiltrates across 11 tumor types. *J. Natl. Cancer Inst.* **108**, djw144 (2016).
11. Laumont, C. M., Banville, A. C., Gilardi, M., Hollern, D. P. & Nelson, B. H. Tumour-infiltrating B cells: immunological mechanisms, clinical impact and therapeutic opportunities. *Nat. Rev. Cancer* **22**, 414–430 (2022).
12. Wouters, M. C. A. & Nelson, B. H. Prognostic significance of tumor-infiltrating B cells and plasma cells in human cancer. *Clin. Cancer Res.* **24**, 6125–6135 (2018).
13. Patil, N. S. et al. Intratumoral plasma cells predict outcomes to PD-L1 blockade in non-small cell lung cancer. *Cancer Cell* **40**, 289–300.e284 (2022).
14. Cabrita, R. et al. Tertiary lymphoid structures improve immunotherapy and survival in melanoma. *Nature* **577**, 561–565 (2020).
15. Helmink, B. A. et al. B cells and tertiary lymphoid structures promote immunotherapy response. *Nature* **577**, 549–555 (2020).
16. Petitprez, F. et al. B cells are associated with survival and immunotherapy response in sarcoma. *Nature* **577**, 556–560 (2020).
17. Tran, H. T. N. et al. A benchmark of batch-effect correction methods for single-cell RNA sequencing data. *Genome Biol.* **21**, 12 (2020).
18. Gao, X. & Cockburn, I. A. The development and function of $CD11c^+$ atypical B cells - insights from single cell analysis. *Front. Immunol.* **11**, 979060 (2022).
19. Holla, P. et al. Shared transcriptional profiles of atypical B cells suggest common drivers of expansion and function in malaria, HIV, and autoimmunity. *Sci. Adv.* **7**, eabg8384 (2021).
20. Horns, F., Dekker, C. L. & Quake, S. R. Memory B cell activation, broad anti-influenza antibodies, and bystander activation revealed by single-cell transcriptomics. *Cell Rep.* **30**, 905–913.e906 (2020).
21. King, H. W. et al. Single-cell analysis of human B cell maturation predicts how antibody class switching shapes selection dynamics. *Sci. Immunol.* **6**, eabe6291 (2021).
22. Calado, D. P. et al. The cell-cycle regulator c-Myc is essential for the formation and maintenance of germinal centers. *Nat. Immunol.* **13**, 1092–1100 (2012).
23. Duan, M. et al. Understanding heterogeneity of human bone marrow plasma cell maturation and survival pathways by single-cell analyses. *Cell Rep.* **42**, 112682 (2023).
24. Wang, X. et al. The role of CXCR3 and its ligands in cancer. *Front. Oncol.* **12**, 1022688 (2022).
25. Wei, Y. et al. B cell heterogeneity, plasticity, and functional diversity in cancer microenvironments. *Oncogene* **40**, 4737–4745 (2021).
26. Cyster, J. G. & Allen, C. D. C. B cell responses: cell interaction dynamics and decisions. *Cell* **177**, 524–540 (2019).
27. Cook, M. E., Jarjour, N. N., Lin, C.-C. & Edelson, B. T. Transcription factor Bhlhe40 in immunity and autoimmunity. *Trends Immunol.* **41**, 1023–1036 (2020).
28. Willis, S. N. et al. Environmental sensing by mature B cells is controlled by the transcription factors PU.1 and SpiB. *Nat. Commun.* **8**, 1426 (2017).
29. Domeier, P. P. et al. IFN-γ receptor and STAT1 signaling in B cells are central to spontaneous germinal center formation and autoimmunity. *J. Exp. Med.* **213**, 715–732 (2016).
30. Jenh, C.-H. et al. Human B cell-attracting chemokine 1 (BCA-1; CXCL13) is an agonist for the human CXCR3 receptor. *Cytokine* **15**, 113–121 (2001).
31. Marques, R. E., Guabiraba, R., Russo, R. C. & Teixeira, M. M. Targeting CCL5 in inflammation. *Expert Opin. Ther. Targets* **17**, 1439–1460 (2013).
32. Haghverdi, L., Buettner, F. & Theis, F. J. Diffusion maps for high-dimensional single-cell analysis of differentiation data. *Bioinformatics* **31**, 2989–2998 (2015).
33. Cao, J. et al. The single-cell transcriptional landscape of mammalian organogenesis. *Nature* **566**, 496–502 (2019).
34. Cortés, M. & Georgopoulos, K. Aiolos is required for the generation of high affinity bone marrow plasma cells responsible for long-term immunity. *J. Exp. Med.* **199**, 209–219 (2004).
35. van Spriel, A. B. et al. The tetraspanin CD37 Orchestrates the α4β1 Integrin–Akt signaling axis and supports long-lived plasma cell survival. *Sci. Signal.* **5**, ra82-ra82 (2012).
36. Rodríguez-Bayona, B., Ramos-Amaya, A., López-Blanco, R., Campos-Caro, A. & Brieva, J. A. STAT-3 activation by differential cytokines is critical for human in vivo–generated plasma cell survival and Ig secretion. *J. Immunol.* **191**, 4996–5004 (2013).
37. Wu, S. Z. et al. A single-cell and spatially resolved atlas of human breast cancers. *Nat. Genet.* **53**, 1334–1347 (2021).
38. Chung, W. et al. Single-cell RNA-seq enables comprehensive tumour and immune cell profiling in primary breast cancer. *Nat. Commun.* **8**, 15081 (2017).
39. Jiao, S. et al. Intratumor expanded T cell clones can be non-sentinel lymph node derived in breast cancer revealed by single-cell immune profiling. *J. Immunother. Cancer* **10**, e003325 (2022).
40. Gao, R. et al. Delineating copy number and clonal substructure in human tumors from single-cell transcriptomes. *Nat. Biotechnol.* **39**, 599–608 (2021).
41. Shiao, S. L. et al. Single-cell and spatial profiling identify three response trajectories to pembrolizumab and radiation therapy in triple negative breast cancer. *Cancer Cell* **42**, 70–84.e78 (2024).
42. Engelhard, V. et al. B cells and cancer. *Cancer Cell* **39**, 1293–1296 (2021).
43. Philip, M. & Schietinger, A. $CD8^+$ T cell differentiation and dysfunction in cancer. *Nat. Rev. Immunol.* **22**, 209–223 (2022).
44. Brechbuhl, H. M. et al. Analysis of circulating breast cancer cell heterogeneity and interactions with peripheral blood mononuclear cells. *Mol. Carcinog.* **59**, 1129–1139 (2020).
45. Pal, B. et al. A single-cell RNA expression atlas of normal, preneoplastic and tumorigenic states in the human breast. *EMBO J.* **40**, e107333 (2021).
46. Xu, K. et al. Single-cell RNA sequencing reveals cell heterogeneity and transcriptome profile of breast cancer lymph node metastasis. *Oncogenesis* **10**, 66 (2021).
47. Tokura, M. et al. Single-cell transcriptome profiling reveals intratumoral heterogeneity and molecular features of ductal carcinoma in situ. *Cancer Res.* **82**, 3236–3248 (2022).
48. Liu, Y.-M. et al. Combined single-cell and spatial transcriptomics reveal the metabolic evolvement of breast cancer during early dissemination. *Adv. Sci.* **10**, 2205395 (2023).
49. Tietscher, S. et al. A comprehensive single-cell map of T cell exhaustion-associated immune environments in human breast cancer. *Nat. Commun.* **14**, 98 (2023).
50. Bassiouni, R. et al. Spatial transcriptomic analysis of a diverse patient cohort reveals a conserved architecture in triple-negative breast cancer. *Cancer Res.* **83**, 34–48 (2023).
51. Moir, S. et al. Evidence for HIV-associated B cell exhaustion in a dysfunctional memory B cell compartment in HIV-infected viremic individuals. *J. Exp. Med.* **205**, 1797–1805 (2008).
52. Wu, C. et al. Lupus-associated atypical memory B cells are mTORC1-hyperactivated and functionally dysregulated. *Ann. Rheum. Dis.* **78**, 1090–1100 (2019).
53. Verstappen, G. M. et al. Gene expression profiling of epithelium-associated $FcRL4^+$ B cells in primary Sjögren's syndrome reveals a pathogenic signature. *J. Autoimmun.* **109**, 102439 (2020).

54. Isnardi, I. et al. Complement receptor 2/CD21− human naive B cells contain mostly autoreactive unresponsive clones. *Blood* **115**, 5026–5036 (2010).

Acknowledgements

We are grateful to the researchers who provided the original data. This work was supported by the National Natural Science Foundation of China: Outstanding Youth Program (No.82322048); National Natural Science Foundation of China: General Program (No.82272872 and 82173184); Natural Science Foundation of Heilongjiang Province of China: Distinguished Youth Program (JQ2023H004); Harbin Medical University Cancer Hospital: Nn10 Plan (Nn102024-02).

Author contributions

Conception and design: T. Liu, G. Yang, X.F. Dai, and C. Qian; Administrative support: T Liu, WZ Wang, and XH Chen; Provision of study materials or patients: D.C. Ji, X.L. Zhang, and F.J. Hu; Collection and assembly of data: X. Cai and J.R. Yang; Data analysis and interpretation: K.X. Liu, X. Li, Y.X. Zhang, and X.F. Dai; Manuscript writing: T. Liu, X. Cai, and J.R. Yang; Final approval of manuscript: All authors.

Competing interests

The authors declare no competing interests.

Additional information

Supplementary information The online version contains supplementary material available at https://doi.org/10.1038/s41523-026-00917-0.

Correspondence and requests for materials should be addressed to Cheng Qian, Xiaofang Dai, Guang Yang or Tong Liu.